La$_{0.7}$Sr$_{0.3}$MnO$_{3 - \delta}$ barrier for Cr$_2$O$_3$-forming SOFC interconnect alloy coated by electrostatic spray deposition

Leandro da Conceição [a,b,*], Laurent Dessemond [b], Elisabeth Djurado [b], E.N.S. Muccillo [a]

[a] Energy and Nuclear Research Institute — IPEN, PO Box 11049, Pinheiros, 05422-970 S. Paulo, SP, Brazil
[b] LEPMI, Laboratoire d'Electrochimie et de Physico-Chimie des Matériaux et des Interfaces, UMR 5279, CNRS, Grenoble INP, Université de Savoie, Université Joseph Fourier, BP75, 38402 Saint Martin d'Hères, France

ABSTRACT

In this work, electrostatic spray deposition (ESD) technology was used to deposit dense, free-cracks and thin La$_{0.7}$Sr$_{0.3}$MnO$_{3 - \delta}$ (LSM) layers on SS446 alloy interconnect to be used in solid oxide fuel cell (SOFC) after subsequent annealing at 800 °C in air for 2 h. The corrosion resistance of uncoated and LSM-coated steels has been studied by electrical and thermogravimetric measurements. The oxidation rate was strongly reduced for LSM-coated steel in ambient air and pure oxygen at 800 °C for 250 h. It was found for the first time that a dense LSM coating as thin as 300 nm efficiently reduces the oxidation rate by limiting outward Cr^{3+} diffusion. A protective chromia scale was detected by SEM and EDS at the interfacial layer. The area specific resistance (ASR) of LSM-coated SS446 was found very low (30 mΩ·cm^2) and stable in comparison with the uncoated one (80 mΩ·cm^2) after 200 h oxidation in air at 800 °C. The results of this work demonstrate the possibility of automated production of dense conductive interconnect LSM-coated materials and give a standard thickness to obtain stable long-term operation.

© 2014 Elsevier B.V. All rights reserved.

1. Introduction

Ferritic stainless steel interconnects for solid oxide fuel cells (SOFC) present several advantages such as enhanced mechanical strength and improved seal efficiency of stacks [1]. However, the high Cr volatility from Cr$_2$O$_3$ formed on the alloy surface results in a chromium poisoning of the SOFC cathode [2] which is typically due to oxide scale formation from volatile gaseous Cr(VI) species such as CrO$_3$ or CrO$_2$(OH)$_2$ [1–3]. At high temperatures, a thermally grown electric conductive chromia-based oxide layer is formed on surface alloys. The chromia scales exhibit poor electrical conductivity [3] which may lead to power loss at the electrode/interconnect interface during long-term SOFC operation. According to literature [3], the outward chromium transport is likely the dominant growth process in the chromia scales whereas the contribution of oxygen transport is substantially smaller. The outward chromium diffusion can result in the formation of voids and cavities at the scale/metal interface leading to poor scale adherence [4]. Thus, after exposure over a thousand hours, the chromia layer can exhibit localized spallation.

To avoid chromium poisoning, a protection oxide coating on the metal interconnect surface can be used and may exhibit low Cr diffusivity at high temperatures. The protection layer is intended to serve as a barrier to both chromium cations and oxygen anion diffusion processes. It can decrease the alloy oxidation kinetics, mitigate or even prevent chromium diffusion from the alloy substrate. This buffer layer is expected to minimize the interfacial area specific resistance (ASR) between the cathode and the interconnect by limiting the growth of the Cr-based oxide scale. The material selected for the protection layer should exhibit high electrical conductivity coupled with low chromium cation diffusivity. Low oxygen ion diffusivity is also required to limit oxidation of the substrate alloy and therefore, the subsequent growth of a chromia or chromia-rich scale or interlayer between the protection layer and the bulk alloy.

Perovskite oxides [5–11] have been applied as protection layer materials because of their high electrical conductivity, close TEC (thermal expansion coefficient) values with stainless steels with a similar structure and composition of the SOFC cathode [12]. They also have the ability to enhance thermo-mechanical integrity. Most of the reports indicate that LSM coatings change the oxidation behavior of base alloys and enhance the long term stability of metallic interconnects. Excellent performances have been reported using protective perovskite coatings between 2 and 40 μm in thickness [13–16]. The ASR for a (La$_{0.80}$Sr$_{0.15}$)$_{0.9}$MnO$_3$ layer (thickness ~ 30 μm) slurry-coated on a Fe–16Cr alloy remained stable at around 74 mΩ·cm^2 for 2600 h at 750 °C in air [9]. An ASR lower than 20 mΩ·cm^2 was recorded after 165 h at 800 °C in air for a plasma-sprayed LSM coating (100 μm thick) on a SS444 substrate [17]. The ASR of (La$_{0.80}$Sr$_{0.20}$)$_{0.98}$MnO$_3$ (less than 100 μm thick)-coated Crofer22APU reached a value of 23 mΩ·cm^2

* Corresponding author at: Energy and Nuclear Research Institute — IPEN, PO Box 11049, Pinheiros, 05422-970 S. Paulo, SP, Brazil. Tel.: +55 11 31339232.
E-mail address: landoufrj@gmail.com (L. da Conceição).

after oxidation for 8000 h at 800 °C in air [10]. However, only a few studies have been devoted to the influence of both, thickness and morphology of the protection coatings on metallic alloys on the chromium diffusion. However, the coating thickness and microstructure fully depend on the fabrication methods. There are numerous techniques for coating metallic interconnects such as chemical vapor deposition, pulsed laser deposition, plasma spraying, screen printing, slurry coating, radio frequency magnetron sputtering, electrodeposition, and sol–gel process [18]. Each technique has its proper advantages and drawbacks. Although these processes are often well known, the ability of monitoring both, thickness and surface morphology of the films is somewhat limited.

The electrostatic spray deposition (ESD) is a relatively simple technique based on electrohydrodynamic laws and does not require expensive equipment or vacuum generation. It also allows an excellent control over the stoichiometry of the film and is therefore an interesting technique in this regard [19]. This technique provides a wide range of very distinct morphologies while conserving strong adhesion to the substrate. An aerosol is created by atomization of a precursor's solution and guided by an electrical field imposed on a metallic nozzle towards a grounded substrate which is normally heated. The shape and spraying modes of the aerosol may be tuned by changing the applied voltage and the physico-chemical properties of the precursor's solution such as surface tension, density and conductivity. The cone–jet mode is the most stable configuration and it can be obtained in a relatively small range of applied voltages [19]. When the electric field is strong enough, the electrostatically stressed liquid surface can be distorted into a stable conical shape (i.e. the Taylor cone, see Fig. 1). A large variety of morphologies can be tailored mainly by the size of the droplets impacting the substrate. Droplet size in the aerosol can vary from ~10 nm to 100 μm [20] depending on the experimental setup. Several studies have modeled how the solution properties and the deposition parameters determine droplet size formed at the nozzle [21]. The most consensual is probably the Gañan–Calvo's relationship [20] (Eq. (1)), showing

that the droplet size varies mainly with the flow rate of the solution and less strongly with the conductivity and surface tension of the solution.

$$d \sim \left(\frac{\rho . \varepsilon_0 . Q^3}{\gamma . \sigma} \right)^{\frac{1}{6}} \tag{1}$$

where d is the droplet diameter (m), ρ is the density (kg·m^{-3}), ε_0 is the vacuum permeability (8.85×10^{-12} F·m^{-1}), Q is the flow rate (m^3·s^{-1}), γ is the surface tension (N·m^{-1}) and σ is the electrical conductivity of the solution (S·m^{-1}).

In this work, La$_{0.7}$Sr$_{0.3}$MnO$_{3-\delta}$ (LSM) layers were prepared by innovative ESD on SS446 steel substrates. The microstructural properties of the LSM protective coating on stainless steels have been optimized varying solution flow rates, nozzle to substrate distance, substrate temperature, the nature of the precursor's solution, and, finally, time deposition. After subsequent annealing at 800 °C in air for 2 h, dense and free-cracks films with controlled thickness were characterized by SEM observations and EDS analysis. The effect of a dense thin LSM coating and the oxide scale on the electrical behavior of uncoated and LSM-coated steels have been investigated. Moreover, aging investigations were performed for 250 h in air at 800 °C for three different LSM thicknesses. One can expect that a dense coating should be more efficient as a diffusion barrier layer than a porous layer. However, there are still controversial arguments in the literature about the effect of coating thickness on the time dependence of ASR [22–29].

2. Experiments

LSM coatings were deposited by ESD on polished ferritic stainless steel SS446 (Ugitech, France) with disc dimensions of 20 mm × 1 mm and the chemical compositions as shown in Table 1. The substrate surfaces were sanded (sandpaper: 600 and 1200 SiC) and polished to eliminate any surface defect and composition variation that could
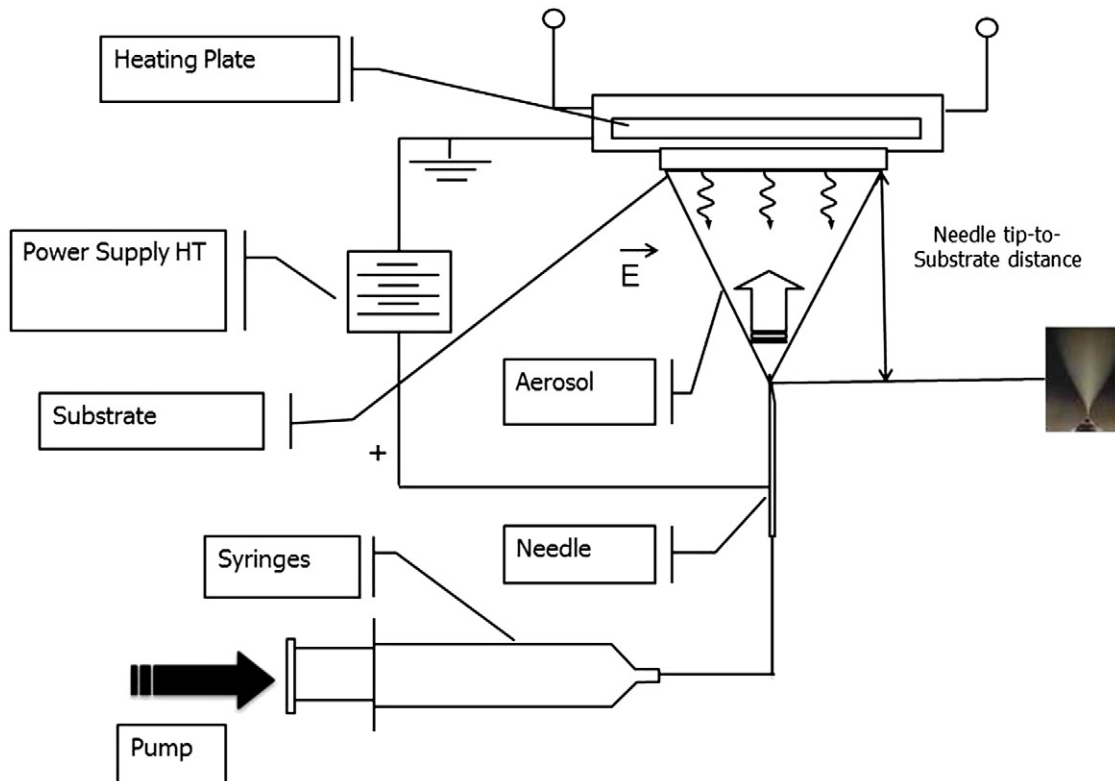

Fig. 1. Sketch of the ESD setup used for film deposition.

Table 1
Chemical composition (wt.%) of ferritic stainless steels used as substrates.

Sample	Fe	Cr	Mn	Si	Mo	V	W	Ni	Cu
SS446	Bal.	23.15	0.53	0.36	0.07	0.11	0.02	0.20	0.15

potentially influence oxidation performance of the alloys. The polished substrates were washed using ultrasound in several steps with deionized water, isopropyl alcohol and acetone during 10 min and were then dried at 100 °C in a furnace.

The LSM-coated SS446 films were deposited using a vertical ESD set-up shown in Fig. 1. The experimental device consists of a syringe pump connected to a hypodermic nozzle that controls the flow rate of the precursor's solution. The substrate is placed above the syringe on a heating plate while a mask is used to define the deposition area. The temperature of the substrate is measured with a K-type thermocouple on the substrate surface without spray. The distance between the nozzle and the substrate can be adjusted. A high-voltage supply is connected to the metallic nozzle and is grounded on the substrate side. The LSM precursor's solution was delivered to the nozzle flow rate at 0.50 mL/h using a Sage™ M361 syringe pump.

The precursor's solutions with a concentration of 0.02 mol·L^{-1} were prepared starting from La(NO$_3$)·6H$_2$O, SrCl$_2$·6H$_2$O and Mn(NO$_3$)$_3$·6H$_2$O in a mixture of 67:33 vol.% ratio of ethanol (C$_2$H$_5$OH, 99.9%) and butyl carbitol (CH$_3$(CH$_2$)$_3$OCH$_2$CH$_2$OCH$_2$CH$_2$OH, 99%) referred to as EtOH and BC, respectively. The boiling points of ethanol and butyl carbitol are equal to 78 and 231 °C, respectively. One deposition was performed with pure ethanol in order to decrease the boiling point of the solution without butyl carbitol. The ESD film deposition conditions concerning the nozzle to substrate distances D, solution flow rate q, deposition time t, and substrate temperature T were initially extracted from a previous report on the deposition of (La$_{0.85}$Sr$_{0.15}$)$_{0.95}$MnO$_{3-\delta}$ on an yttria stabilized zirconia substrate [30]. The deposition temperature was referred to the substrate surface facing the solution spray, obtained after temperature calibration with a type K thermocouple. Positive high voltages of approximately 8 kV were used and applied for proper aerosol generation and spray stabilization for each sample. The LSM depositions were performed in the following ranges for the substrate temperature T, the nozzle to substrate distance D, the flow rate q and the deposition time t: T = 300, 450 and 500 °C, D = 20, 40 and 50 mm, q = 0.34, 0.50 and 0.67 mL/h, t = 15, 30 and 60 min. All raw coatings were found amorphous and a subsequent annealing at 800 °C for 2 h in air was sufficient for the crystallization of LSM films.

The oxidation behavior of uncoated and LSM-coated SS446 alloys was studied by monitoring the weight change in air and in pure oxygen at 800 °C for 250 h. Heating and cooling rates were 2 °C/min. The furnace was cooled down, and the samples were balanced in an interval of 50 h until 250 h. The average mass change was calculated from individual mass gains of coated and uncoated samples. The weight gain after each thermal cycle was measured with an accuracy of 10^{-4} g. The gas flow rate was kept constant at 6 L·h^{-1} during the test.

The phase formation was characterized by X-ray diffraction (XRD) using a PANalytical X'Pert Pro MPD diffractometer, from 10 to 90° 2θ range with a speed of 2°min^{-1}. The morphology and chemical composition of the films were analyzed by scanning electron microscopy using a field-emission gun ZEISS Ultra 55 coupled with energy dispersive X-ray analyzer ZEISS 1540XB (Carl Zeiss NTS GmbH, Germany).

The ASR of uncoated and LSM-coated Fe–Cr alloys was measured as a function of time (up to 200 h) at 800 °C in air by using a DC two-point, four-wire probe. In order to avoid any penetration of the metal electrode through the thin LSM dense coatings, platinum meshes were used as current collectors. A constant load (100 g) was applied to achieve the better contact area of the current collectors and investigated samples. Meshes were chosen instead of paste because some studies [31,32] have shown that contacting with platinum paste not only modifies the thickness of the oxide scale formed but also the recorded

resistance. A constant current from 1 to 10 mA was passed through Pt probes and the voltage in the sample was measured using a multimeter (HP 34401A). In parallel, the electric behavior of LSM-coated SS446 samples was evaluated during thermal cycles between 800 and 50 °C for up to approximately 300 h.

During oxidation at high temperature, the ASR of uncoated and LSM-coated alloys is affected by the resistivity of the interfacial oxide layer. By exposing alloys at high temperature, oxide scale forms on both sides of the substrate. The ASR was calculated according to Ohm's law: ASR = V / 2i, where V is the voltage drop and i the current density. A factor of 2 was added to take into account that the voltage drop was measured across two scales connected in series. The area was chosen equal to the geometric area covered by platinum meshes according to high conductivities of stainless steel substrates and LSM coating. ASR measurements during oxidation at 800 °C in air were performed twice on all samples. The ASR values varied within less than 10% in the chosen experimental conditions.

3. Results and discussion

3.1. Microstructure

3.1.1. Uncoated alloys

Fig. 2 depicts the XRD pattern of uncoated SS446 steel after annealing for 250 h. The main diffraction peaks of the ferritic SS446 steel are detected. Through XRD analysis, it is observed that the oxides formed on the alloy surface are mainly composed of Cr$_2$O$_3$ (ICSD − 381479) and (Cr,Mn)$_3$O$_4$ (ICSD − 330895) with a spinel structure. We can observe that there is an increase in the intensity of the peaks of chromium oxide, suggesting that pure (and most likely thicker) oxygen Cr$_2$O$_3$ scale is formed on (Cr, Mn)$_3$O$_4$.

The surface micrographs of uncoated SS446 substrates exposed to air and pure oxygen atmospheres at 800 °C for 250 h are shown in Fig. 3. A prism shaped surface with a typical pyramid structure, characteristic of a spinel (Mn–Cr) crystalline phase, can be observed. After oxidation in pure oxygen (Fig. 3(b)), the layer presents some flaws in the presence of aggregates with finer microstructures between the prism shaped particles. This can be attributed to spallation of the oxidized layer. Indeed, a high partial oxygen pressure at the oxide/alloy interface can alter the inward diffusion of oxygen and the adherence of the layer. The lower contents of manganese and iron after oxidation in pure oxygen are in agreement with this assumption. A spinel (Mn–Cr) crystalline phase, covering an inner chromia layer with smaller grains, has already been evidenced after oxidation at high temperatures in air [33–37]. The oxidation process of Fe–Cr alloys containing
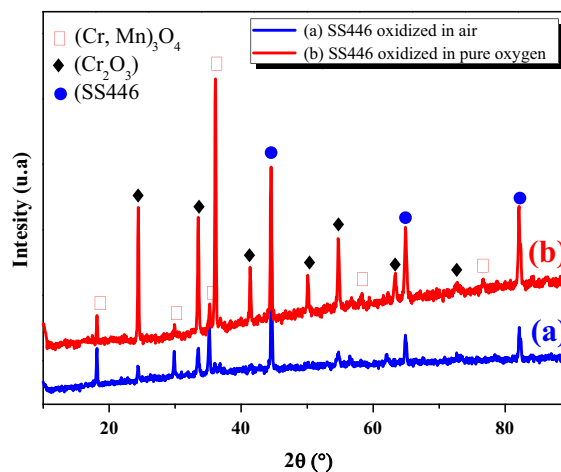

Fig. 2. XRD patterns of the uncoated SS446 samples oxidized at 800 °C for 250 h (a) in air and (b) pure oxygen.
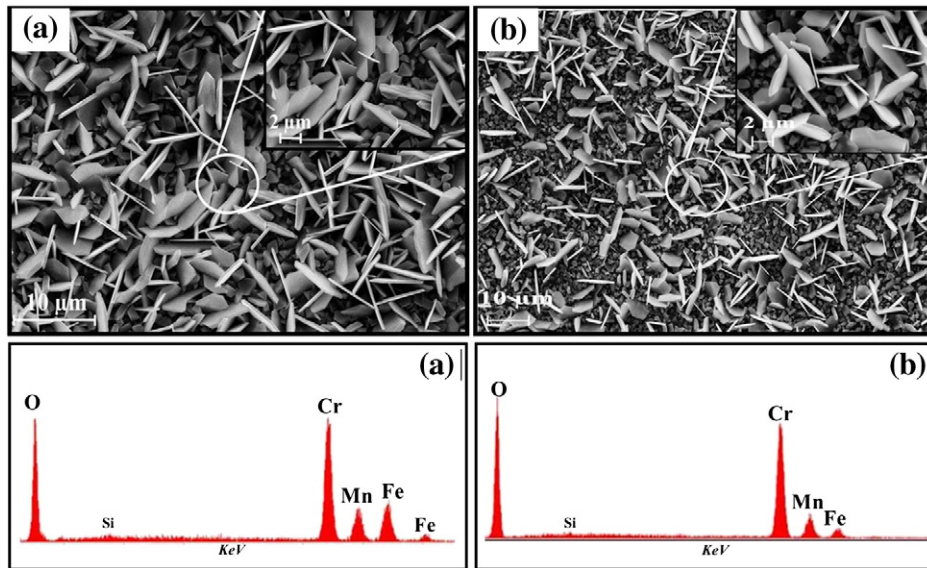
Fig. 3. SEM images of the uncoated surface of SS446 samples oxidized at 800 °C for 250 h (a) in air and (b) pure oxygen.

manganese is controlled by the outward diffusion of cations through the well-developed oxide scale [38–41]. Manganese ions diffuse faster than chromium ions in the oxide scale resulting in a double layered oxide scale with Mn–Cr spinel on top of the chromia layer. The Mn content in the surface spinel is an increasing function of that of the alloy. Moreover, no Mn-containing oxide was detected after oxidation of a Mn-free alloy [42]. Accordingly, the Mn rich surface oxide is likely to originate from a fast diffusion of manganese ions across the oxide scale.

3.1.2. LSM-coated alloys before long term oxidation

As mentioned above and based on a previous study [30], the ESD deposition parameters must be optimized for a metallic substrate to control the morphology of the LSM film.

As shown in Fig. 4, a dense morphology accompanied by large cracks was obtained by using a short nozzle to substrate distance with a large flow rate and a low deposition temperature (Sample (1)). The formation of these cracks is assigned to the large amount of liquid droplets favoring low temperature evaporation according to Eq. (1) [43]. Then, a lower solution flow rate (0.34 mL/h) was used with a larger nozzle to substrate distance (50 mm) while the substrate temperature was increased from 300 to 450 °C. Thus, cracks were removed due to a rapid solvent evaporation but the presence of smaller and drier droplets resulted in a granular morphology (Sample (2)). At this stage, a compromise must be found to increase the compactness of the film in order to compensate the lack of dense morphology. This is why the same distance of 50 mm, a flow rate of 0.67 mL/h and a temperature of 500 °C were applied for Sample (3) using pure ethanol to prevent an excess of liquid in the droplets according to its lower boiling point. A porous layer with a "coral" type microstructure was obtained because the droplets arriving on the substrate still contained a low amount of solvent and were attracted by preferential landing when impacting the substrate [43]. Accordingly, the droplet size must be increased for a better spreading on the substrate by reducing the nozzle to substrate distance to an intermediate value of 40 mm and by reducing the substrate temperature from 500 to 450 °C to decrease their evaporation rate during flight [44]. The flow rate was adjusted to 0.50 mL/h to avoid any excess of liquid impacting the substrate. In these conditions, a dense and homogeneous LSM film, free of cracks was obtained using a mixture of ethanol and butyl carbitol (Sample (4)).

By using these optimized deposition parameters, the LSM thickness was adjusted by varying the depositing time between 15 and 60 min.

After deposition for 15 min at 450 °C and subsequent annealing at 800 °C for 2 h, the surface of a LSM-coated SS446 alloy shows typical pyramidal particles of similar size (Fig. 4a) which is characteristic of a spinel crystalline structure [45]. The direct observation of these oxides can be related to a breakdown of the thin LSM coating (less than 100 nm) (Fig. 4b). This is likely due to non-uniform coating after 15 min deposition time by ESD. Thus, such a layer is not efficient to hinder cations diffusion. For longer deposition times, the LSM coatings present a more homogeneous surface, almost dense and free of cracks (Fig. 4).

When the ESD deposition time was increased by a factor of 2 (from 30 to 60 min), the LSM thickness is not strongly increased (from 280 to 300 nm) while the increase in the deposition time from 15 to 30 min almost led to a threefold increase of the thickness (from 100 to 280 nm) (Fig. 5). However, the LSM film appears denser with a flat surface after deposition for 60 min. It seems that during the very first moments of coating formation, the first droplets impact the smooth polished substrate with an equilibrium between the incoming solution and the solvents' evaporation on the hot substrate. This leads to a dense and very thin film due to a spreading on a smooth surface. As far as the process continues up to 15 min, the incoming droplets preferentially land on the top of already existing highest points of the layer surface because these parts act as concentrators of the electrical field lines on the surface of the substrate (this phenomenon can be referred to as "preferential landing" [43,44]). Hence, an increased roughness of the coating is observed. An increased porosity is formed in particular when deposition time is increased up to 30 min. Then, the arriving liquid droplet excess penetrates by capillary action (Fig. 5(e)) into the formed pores in the sublayer and consequently fills the porous microstructure leading to a dense film. A clear more compact microstructure has been obtained after 60 min keeping the thickness almost constant.

3.1.3. LSM-coated alloys after long-term oxidation

After oxidation at 800 °C for 250 h in air, some cracks are observed on the surface of SS446 alloy coated by a thin LSM film (Fig. 5a), which is not so surprising since surface cracks were evidenced before oxidation (Fig. 4). The faceted grains located between the LSM grains are related to duplex Cr_2O_3 and/or $(Cr, Mn)_3O_4$ phases [6,11] as confirmed by EDS analysis (Fig. 6a). Since LSM is crystallized after 2 h at 800 °C, the crackling of the coating could originate from a thermal expansion mismatch between the alloy and thin LSM film [5,45,46], yielding the development of compressive residual stresses in the film
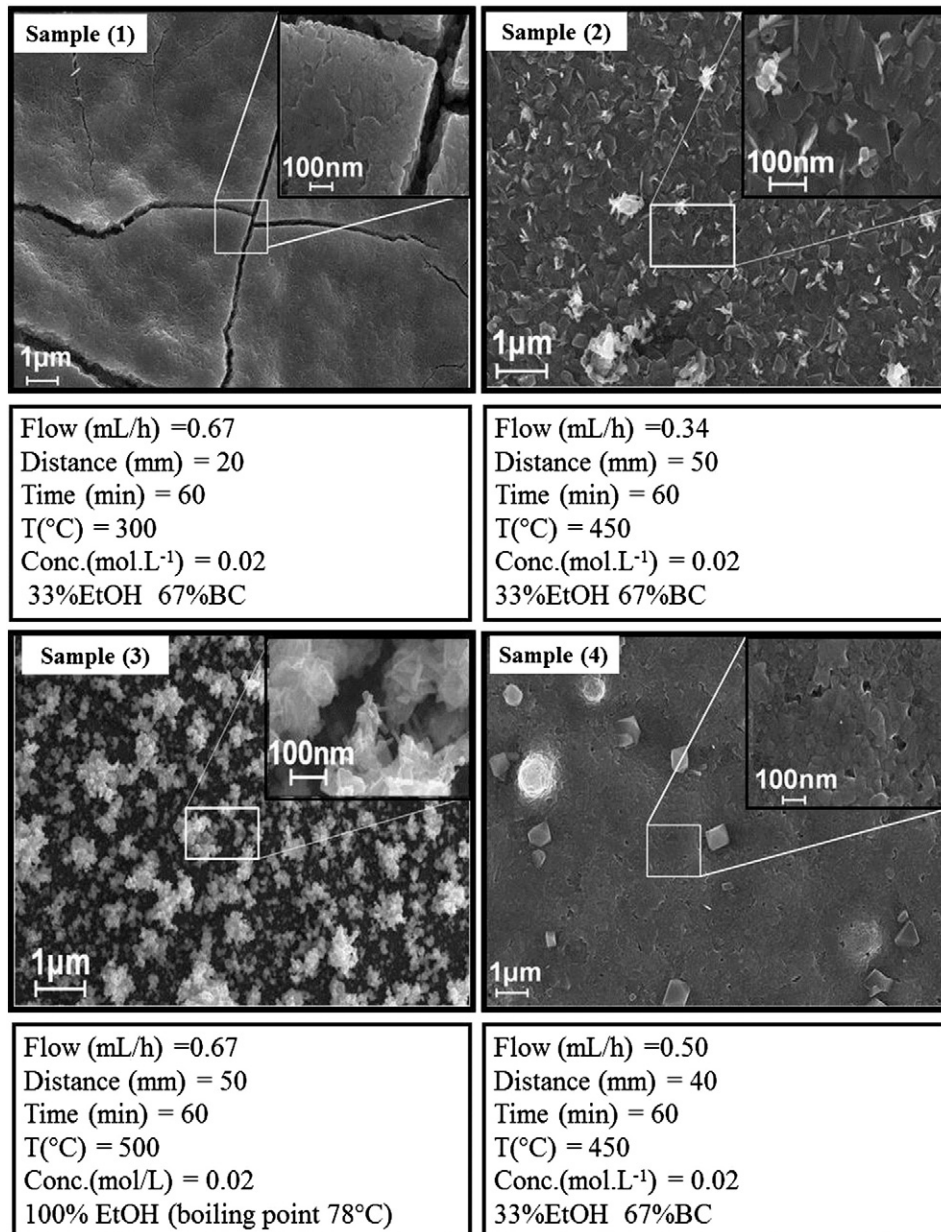
Fig. 4. Morphology of thin LSM films coating on SS446 alloy and annealed at 800 °C for 2 h in air.

during the cooling process [47]. The EDS analysis also revealed the existence of iron oxides in the outer layer (Fig. 6a). Such oxides are more permeable to oxygen and, thus, favor the thickening of the chromium-based layer [48].

For thicker LSM films, no cracks are evidenced on the surface of the coated alloys, suggesting a better adherence of the coatings. For a 280 nm thick LSM film, the formation of Cr_2O_3 and/or $(Cr, Mn)_3O_4$ phases on the surface is confirmed by EDS (Fig. 6b). The existence of small pores in the film is likely to favor both chromium and oxygen diffusion processes [6]. Due to a low open porosity (Fig. 3), no chromium-based oxides are detected on the surface of the alloy coated by a 300 nm thick LSM film (Fig. 6). After 200 h of oxidation no thickness variation of the Cr_2O_3 and/or $(Cr, Mn)_3O_4$ layers was detected, proving that this coating is efficient as a diffusion barrier layer for chromium. It is worthy to note that the high intensities of oxide scale peaks (Fig. 6c) are likely due to the fact that the penetration depth of X-rays is higher than the LSM thickness.

3.2. Weight gain investigation

Uncoated and LSM-coated SS446 alloys exhibited a near parabolic oxidation behavior for 250 h at 800 °C in air and pure oxygen (Fig. 7). The parabolic rate law was verified by plotting the ratio of the weight gain Δm to the total oxidized area S versus the square of the oxidation time t. The corresponding slopes enabled the calculation of the apparent parabolic rate constant K_p [1,36]. The result indicates a diffusion controlled oxidation process [49,50]. Since chromium oxide and manganese–chromium spinel phase are the main reaction products (Figs. 5 and 6), K_p can be seen as a combination of O^{2-}, Cr^{3+} and $Mn^{2+/3+}$ diffusivities in such oxides.

The first obvious result from Fig. 7 is that coating a SS446 alloy by a LSM film decreased the mass gain during long term oxidation at high temperatures, regardless of both, film thickness and aging atmosphere which is in agreement with literature data [51,52]. This also corresponds to previous reports on Crofer22APU coated by $La_{0.85}Sr_{0.15}MnO_3$-based
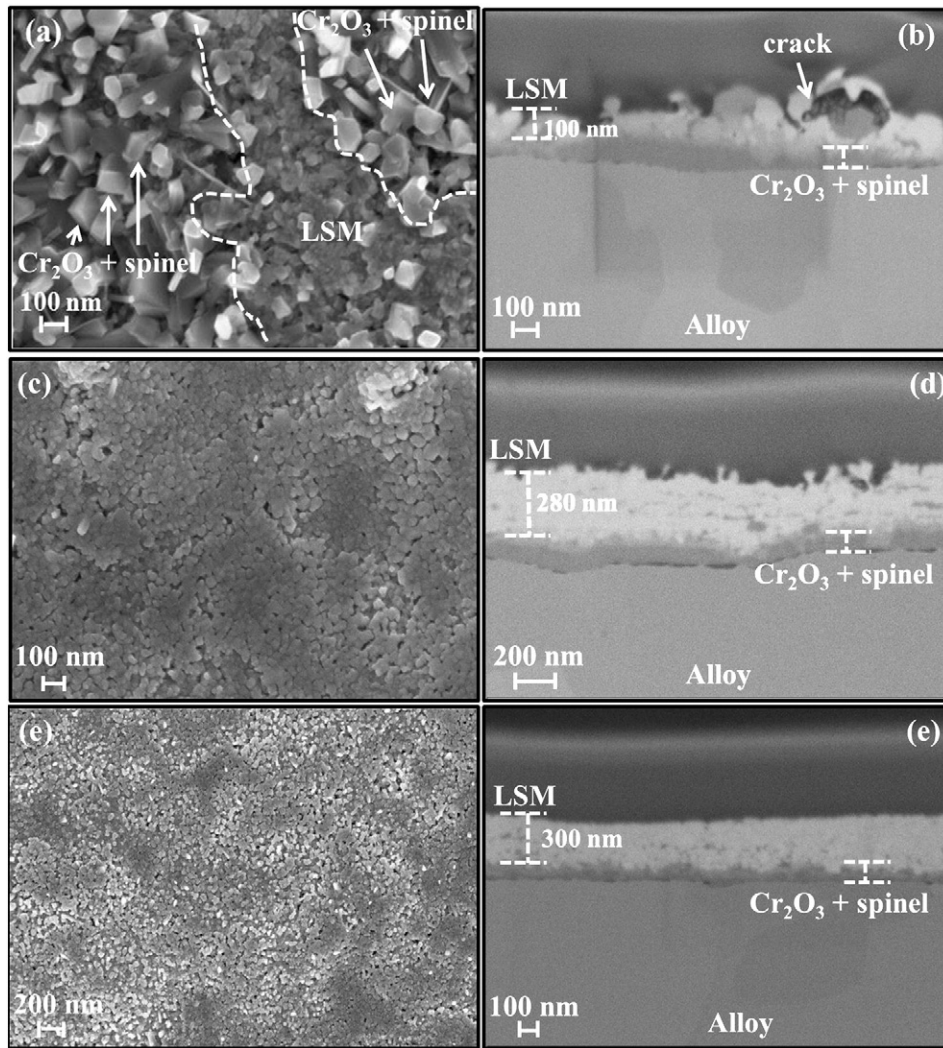
Fig. 5. SEM images of the surface and cross sections of LSM-coated SS446 with different thicknesses: (a), (b) 100 nm; (c), (d) 280 nm and (e), (f) 300 nm.

films with thicknesses higher than 15 μm deposited by plasma spraying [49] or slurry coating [53]. The recorded decrease of weight gain is an increasing function of the LSM thickness at 800 °C. No gain was evidenced by Persson et al. [53] at 900 °C in humidified air after 4000 h by increasing the LSM thickness from 15 to 30 μm. For an uncoated alloy, the apparent rate constant is equal to $2.6 \ 10^{-13} \ g^2 \cdot cm^{-4} \cdot s^{-1}$ at 800 °C (Fig. 8) which is rather to previously reported values for such commercial stainless steel treated at this temperature (1.3–$2.0 \ 10^{-13} \ g^2 \cdot cm^{-4} \cdot s^{-1}$) [36, 54]. At this stage, one can note that the K_p values are higher than those determined for Crofer22APU alloy of rather close chromium contents, for instance 4–$8 \ 10^{-4} \ g^2 \cdot cm^{-4} \cdot s^{-1}$ at 800 °C in air [38,55,56]. However, these values are significantly lower than other reported values for this alloy [57]. Nonetheless, one must keep in mind that the oxidation behavior of ferritic stainless steels depends on the chromium contents and alloying elements [31,58,59].

After deposition of a 100 nm thick LSM film, the apparent rate constant decreases down to $1.5 \ 10^{-13} \ g^2 \cdot cm^{-4} \cdot s^{-1}$ at 800 °C in air, indicating a partial hindering of the growth of the oxide scale. Nevertheless, this coating cannot be viewed as totally efficient because LSM was not evenly distributed on the alloy surface before long term oxidation. Therefore, the inward oxygen diffusion was not fully hindered. An argument in favoring this assumption is that the mass gain and K_p are lower when depositing thicker LSM layers (Figs. 7 and 8). The apparent rate constant is then lower than $4 \ 10^{-14} \ g^2 \cdot cm^{-4} \cdot s^{-1}$ at 800 °C in air. As these layers are evenly distributed on the sample

surface (Fig. 5), the recorded decrease indicates that these coatings acted as a transport barrier for oxygen by reducing the oxygen partial pressure at the LSM/oxide scale interface. Accordingly, the driving force for the inward oxygen diffusion is decreased and the parabolic rate constant is reduced [49]. This suggests that the oxidation process becomes more controlled by outward diffusion of cations through the oxide scale, since the cation diffusion coefficients are higher than that of oxygen [60,61].

The oxidizing atmosphere has an effect on the oxidation behavior (Fig. 7). A higher mass increase was observed in oxygen compared to air, except for a 100 nm thick LSM film. The origin of this behavior remains unclear. The increase of K_p in oxygen is lower than those recorded for uncoated and LSM-coated chromia-forming steels [49]. Since one can assume that a limited access to oxygen at the surface of the growing oxide scale is expected, the increase of the oxidation rate with the oxygen partial pressure can be related to enhanced cation diffusion [49]. At this stage, it is worth to mention that, according to our knowledge, it is the first time that a dense LSM film of 300 nm thickness acts as an efficient barrier to hinder the growth of the oxide scale.

3.3. ASR investigation

The ASR variations versus oxidation time at 800 °C in air for all investigated specimens are shown in Fig. 9. For the uncoated alloy, the initial decrease of ASR during ~10 h can be due to enhanced contacts with the current collector. Indeed, since platinum meshes were used for
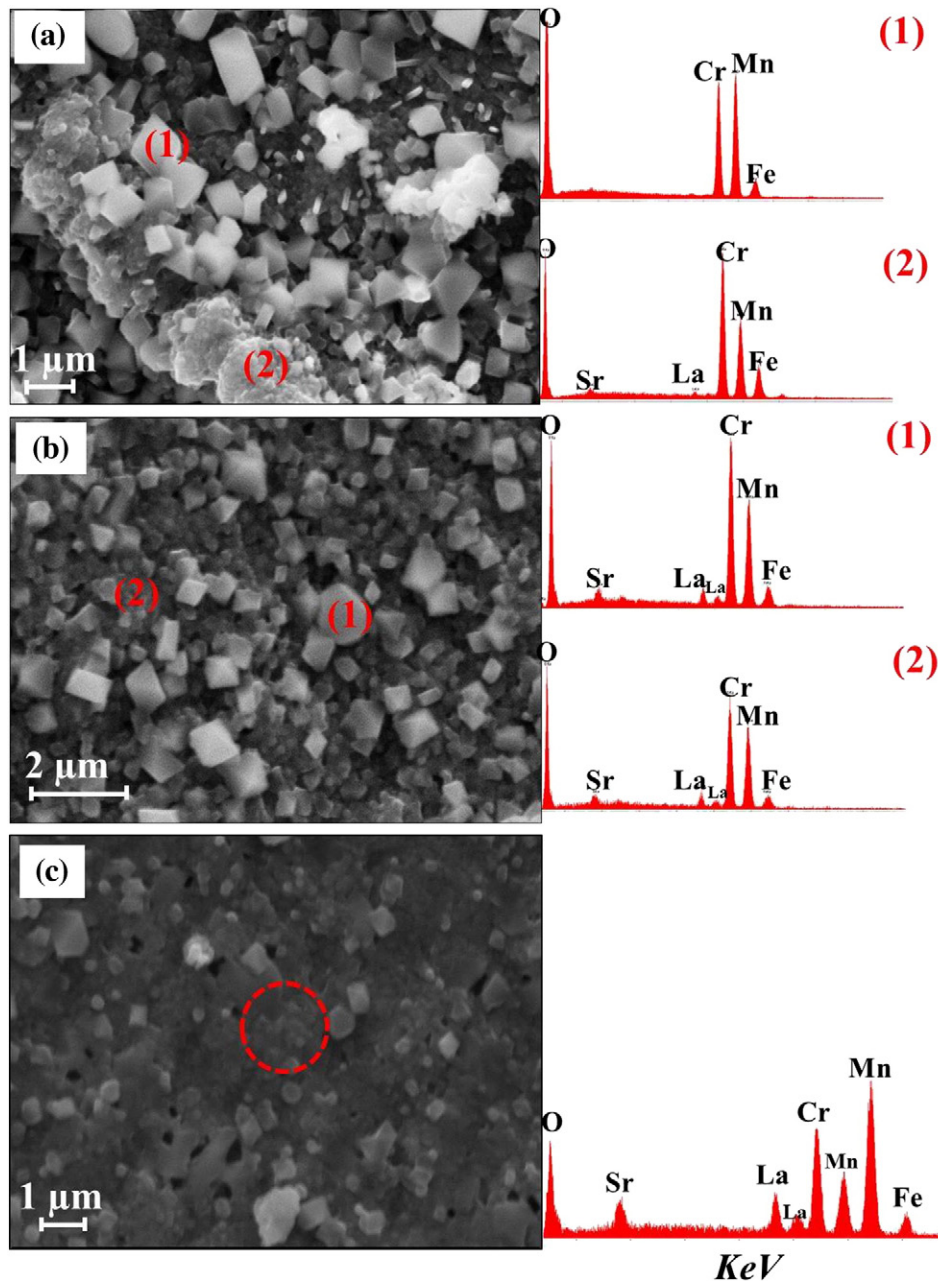
Fig. 6. SEM images and EDS analysis of the surface of LSM-coated SS446 with different thicknesses after oxidation at 800 °C during 250 h in air: (a) 100 nm, (b) 280 nm and (c) 300 nm.

current collection, no penetration of platinum in the growing oxide scale can be invoked in the chosen experimental conditions. For longer aging times, the ASR steadily increases versus the oxidation time, as already observed for uncoated ferritic stainless steels with nearly similar chromium contents than SS446 alloy [10,14,15,27,45,62–65]. This increase can be related to the continuous growth of the oxide scale on the substrate surface. After 200 h at 800 °C in air, the ASR of uncoated alloy is lower than 80 mΩ·cm², value higher than those reported in literature under the same experimental conditions (<40 mΩ·cm²). This difference can originate from high silicium content (Table 1) yielding the formation of insulating silicon precipitates [66] as seen by EDS analysis (Fig. 3). The ASR of an uncoated ZMG232 alloy containing 0.16 wt.%, the Si content was higher than that recorded for uncoated Crofer22APU alloy containing 0.03 wt.% Si by a factor of 1.6 after 200 h at 800 °C in air [5].

During the first 50 h of oxidation, the ASR of LSM-coated alloys decreases regardless to the coating thickness. This is in contradiction

with some previously published results. There, the recorded steady increase of ASR is attributed to the continuing growth of the oxide scale on the substrate surface [10,11,14,27,45,63,67]. However, the decrease of the ASR of coated-stainless steels during oxidation at 800 °C in air was also reported [68]. For instance, the decreasing ASR of Crofer22APU alloys coated by reactive element oxides was related to the formation of perovskite oxides with the chromia growing layer which has a good conductivity at high temperature [55]. Since the LSM films, deposited by ESD, are well crystallized before aging at 800 °C and by considering the high compactness of these films (Fig. 5), the decrease of ASR is not likely due to a continuous sintering of the protection layers; at least for the two thicker films. Accordingly, the recorded decrease can be related to increased contact area between the current collectors and LSM deposited to the formation of a structure of higher conductivity [56,59], i.e. a spinel phase. An argument which supports this assumption is that the ASR remains nearly unchanged for oxidation times higher than 150 h and is lower than its initial value. This indicates that the spinel layer
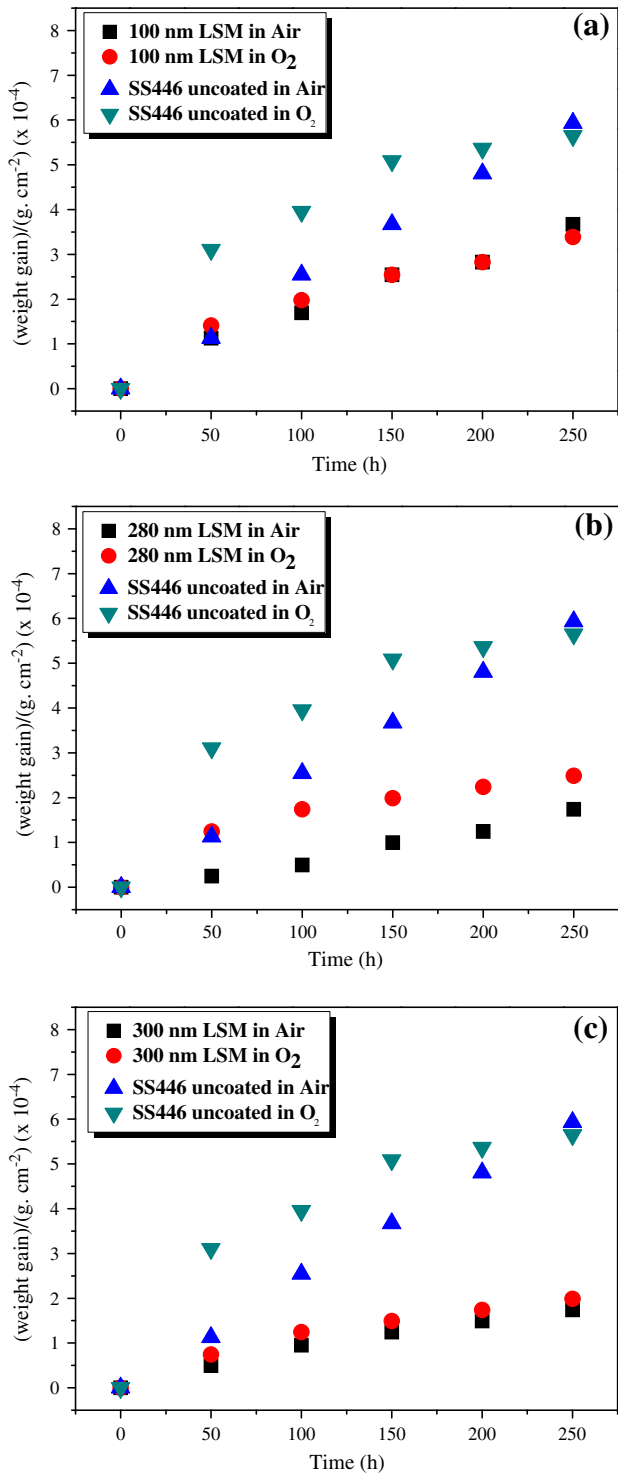
Fig. 7. Oxidation kinetics of uncoated and LSM-coated SS446 in air and pure oxygen with different thicknesses: (a) 100 nm, (b) 280 nm and (c) 300 nm.

Fig. 8. Parabolic rate constants determined for uncoated and LSM-coated SS446 alloys after 250 h at 800 °C in air and pure oxygen.

reach an average value slightly higher than that recorded after 100 h (Fig. 9).

To gain additional information on the electric behavior of the investigated assemblies, the ASR was measured between 600 and 900 °C before and after long term oxidation at 800 °C in air. Between 600 and 900 °C, the logarithm of (ASR/T) varies linearly versus the reciprocal temperature (1/T) regardless of the sample (Fig. 9B). The corresponding activation energy (E_a) was calculated from the slope of the recorded linear curves and values are reported in Table 2. At a given temperature,

Fig. 9. Area specific resistance as a function of oxidation time at 800 °C in air (a) and Arrhenius plots recorded before and after oxidation during 200 h at 800 °C in air (b) of LSM-coated SS446 alloys (a) 100 nm, (b) 280 nm and (c) 300 nm and (d) uncoated SS446 alloy.

compensates the continuous growth of chromia. A peculiar behavior was observed for the 100 nm thick LSM film between 100 and 140 h at 800 °C in air (Fig. 9). This is not linked to the experimental conditions because it was recorded for two similar samples. The sudden increase in ASR is not likely due to a partial spallation of the oxide layer, grown at 800 °C [69,70], but rather to a partial cracking of the LSM film during oxidation, thus enhancing the growth of the oxide scale (Fig. 5). The further formation of the spinel phase allows the increase of the contact area with the current collectors and results in a decreasing ASR to
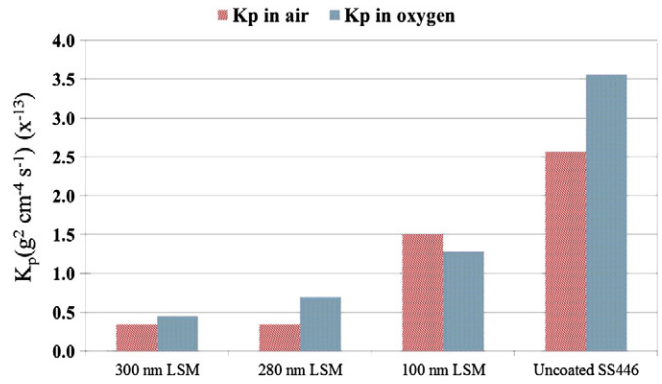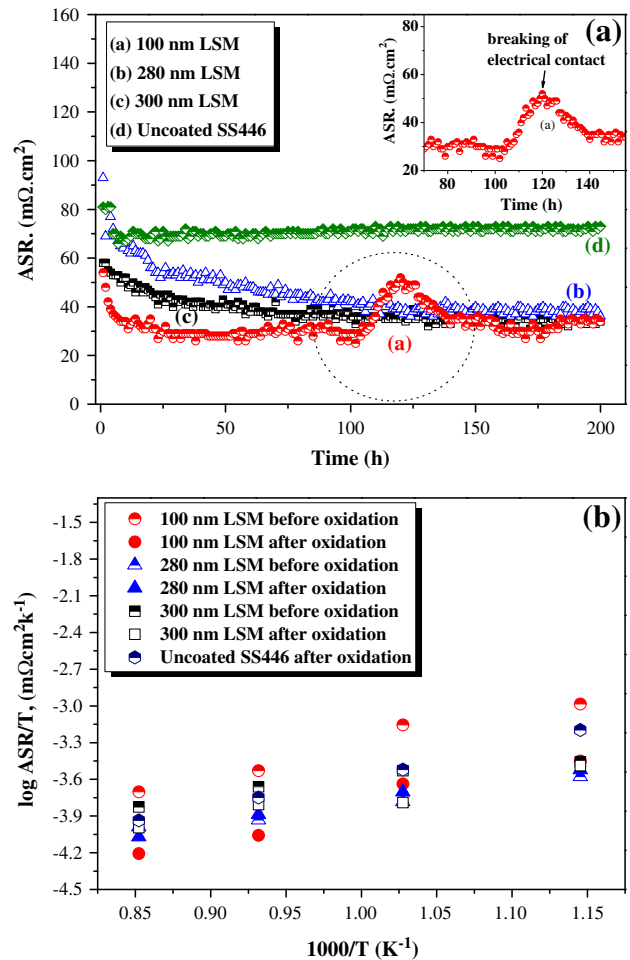
Table 2
Activation energy for ASR of uncoated and LSM coated SS446 before and after oxidation during 200 h at 800 °C in air (600 °C ≤ T ≤ 900 °C).

Sample	E_a (eV) Before oxidation	E_a (eV) After oxidation
Uncoated SS446	–	0.58
100 nm LSM-coated	0.50	0.55
280 nm LSM-coated	0.28	0.36
300 nm LSM-coated	0.38	0.40

the ASR values are in good agreement with the variations recorded during isothermal oxidation. These values are close for all LSM-coated alloys after oxidation. Moreover, the ASR is lower in average after long term oxidation. It is worthy to note that the activation energy for LSM-coated samples is not strongly modified after long term oxidation, indicating that the conduction process remains nearly unchanged. The values of activation energy are in the order of those determined for LSM-coated SS444 alloys [17]. The results suggest that the electric behavior of coated alloys is not monitored by the LSM layer because the activation energy for conduction in LSM is low (~0.10 eV) under the chosen experimental conditions [1]. Since the activation energy for conduction in the spinel phases (>0.80 eV) are higher than that of chromia (~0.30 eV), the electric behavior of all investigated assemblies are dominated by chromium oxides which represent the low conducting phase.

The ASR of LSM-coated alloys was also recorded during thermal cycles between 800 and 50 °C after long term oxidation at 800 °C in air. The heating and cooling rates were equal to 10 °C/min. An example of the corresponding variations is given in Fig. 10 for a 300 nm thick LSM coating. As expected from the thermal activation of the electric behavior of ASR (Fig. 9), there is a decreasing function of the measured temperature. After 6 subsequent thermal cycles, no significant variation of the ASR was recorded at the two reference temperatures. This clearly shows the high adherence of LSM films on the chosen alloy and that the microstructure of this protection layer is efficient to provide a strain tolerance and improved thermo-mechanical stability during the SOFC operation.

4. Conclusions

The presented results show that thin 300 nm LSM coatings are efficient for lowering the oxide scale growth rate of SS446 stainless steel alloys at high temperature in both air and pure oxygen atmosphere. For the 300 nm LSM-coated sample, the great ASR performance is due to an excellent adhesion of the LSM film on the oxide scale and also to the high density of LSM film after 200 h of oxidation. The densified thin LSM-coating layer does not only significantly decrease the contact resistance between the interfacial spinel, oxide scale, and the steel interconnect, it can also act effectively as a barrier to outward diffusion of chromium cations, thus preventing subsequent chromium migration into the cathode and contact material. Electrostatic spray deposition can be seen as an alternative to other deposition methods since this technique shows good reproducibility and excellent efficiency to obtain nanometric layers on the interconnect surface, which is fundamental to decreasing the cost of manufacturing of ceramic protective coatings on SOFC interconnects. The thin LSM coating has a further advantage of being sufficiently electrically conductive and chemically compatible with other ceramic components of SOFC. Furthermore, it may provide beneficial elements for the scale growth (manganese and lanthanum).

Acknowledgments

References

[1] J.W. Fergus, R. Hui, X. Li, D.P. Wilkinson, J. Zhang, Solid Oxide Fuel Cells: Materials Properties and Performance, CRC Press, Boca Raton, 2009. 179–212.
[2] K. Hilpert, D. Das, M. Miller, J. Electrochem. Soc. 143 (1996) 3642–3647.
[3] J.W. Fergus, Mater. Sci. Eng. A 397 (2005) 271–283.
[4] P.Y. Hou, J. Stringer, Mater. Sci. Eng. A 202 (1995) 1–10.
[5] C. Chu, J. Lee, T. Lee, Y. Cheng, Int. J. Hydrog. Energy 34 (2009) 422–434.
[6] L. Da Conceição, L. Dessemond, E. Djurado, M.M.V.M. Souza, J. Power Sources 241 (2013) 159–167.
[7] L. Da Conceição, M.M.V.M. Souza, Thin Solid Films 534 (2013) 218–225.
[8] H. Hwang, G.M. Choi, J. Electroceram. 22 (2008) 67–72.
[9] J. Kim, R. Song, S. Hyun, Solid State Ionics 174 (2004) 185–191.
[10] S.-S. Pyo, S.-B. Lee, T.-H. Lim, R.-H. Song, D.-R. Shin, S.-H. Hyun, Y.-S. Yoo, Int. J. Hydrog. Energy 36 (2011) 1868–1881.
[11] M.-J. Tsai, C.-L. Chu, S. Lee, J. Alloys Compd. 489 (2010) 576–581.
[12] V.I. Gorokhovsky, P.E. Gannon, J. Wallace, D. VanVorous, C. Bowman, M.C. Deibert, R. J. Smith, J. Electrochem. Soc. 158 (2011) B526–B535.
[13] H.W. Nie, T.-L. Wen, H.Y. Tu, Mater. Res. Bull. 38 (2003) 1531–1536.
[14] S. Lee, C.-L. Chu, M.-J. Tsai, J. Lee, Appl. Surf. Sci. 256 (2010) 1817–1824.
[15] Q. Fu, D. Sebold, F. Tietz, H.-P. Buchkremer, Solid State Ionics 192 (2011) 376–382.
[16] J.-J. Choi, J. Ryu, B.-D. Hahn, W.-H. Yoon, B.-K. Lee, J.-H. Choi, D.-S. Park, J. Alloys Compd. 492 (2010) 488–495.
[17] D.P. Lim, D.S. Lim, J.S. Oh, I.W. Lyo, Surf. Coat. Technol. 200 (2005) 1248–1251.
[18] N. Shaigan, W. Qu, D.G. Ivey, W. Chen, J. Power Sources 195 (2010) 1529–1542.
[19] A. Princivalle, E. Djurado, Solid State Ionics 179 (2008) 1921–1928.
[20] A.M. Ganan-Calvo, J. Davila, A. Barrero, J. Aerosol Sci. 28 (1997) 249–275.
[21] O. Wilhelm, L. Mädler, S.E. Pratsinis, J. Aerosol Sci. 34 (2003) 815–836.
[22] F. Changjing, S. Kening, Z. Derui, J. Rare Earths 24 (2006) 320–326.
[23] X. Deng, P. Wei, M.R. Bateni, A. Petric, J. Power Sources 160 (2006) 1225–1229.
[24] L. Chen, N. Magdefrau, E. Sun, J. Yamanis, D. Frame, C. Burila, Solid State Ionics 204–205 (2011) 111–119.
[25] D.-J. Jan, C.-T. Lin, C.-F. Ai, Thin Solid Films 516 (2008) 6300–6304.
[26] J.-J. Choi, D.-S. Park, B.-D. Hahn, J. Ryu, W.-H. Yoon, J. Am. Ceram. Soc. 91 (2008) 2601–2606.
[27] C. Chu, J. Wang, S. Lee, Int. J. Hydrog. Energy 33 (2008) 2536–2546.
[28] Z.J. Feng, C.L. Zeng, J. Power Sources 195 (2010) 4242–4246.
[29] C.J. Fu, K.N. Sun, N.Q. Zhang, X.B. Chen, D.R. Zhou, Thin Solid Films 516 (2008) 1857–1863.
[30] A. Princivalle, D. Perednis, R. Neagu, E. Djurado, Chem. Mater. 16 (2004) 3733–3739.
[31] X. Montero, F. Tietz, D. Stöver, M. Cassir, I. Villareal, Corros. Sci. 51 (2009) 110–118.
[32] K. Huang, P.Y. Hou, J.B. Goodenough, Solid State Ionics 129 (2000) 237–250.
[33] K. Ogasawara, H. Kameda, Y. Matsuzaki, T. Sakurai, T. Uehara, A. Toji, N. Sakai, K. Yamaji, T. Horita, H. Yokokawa, J. Electrochem. Soc. 154 (2007) B657–B663.
[34] W.J. Quadakkers, J. Pirón-abellán, V. Shemet, Mater. Res. 7 (2004) 203–208.
[35] Y. Larring, R. Haugsrud, T. Norby, J. Electrochem. Soc. 150 (2003) B374–B379.
[36] Z. Yang, K.S. Weil, D.M. Paxton, J.W. Stevenson, J. Electrochem. Soc. 150 (2003) A1188–A1201.
[37] B. Hua, J. Pu, W. Gong, J. Zhang, F. Lu, L. Jian, J. Power Sources 185 (2008) 419–422.
[38] Z. Yang, M.S. Walker, P. Singh, J.W. Stevenson, T. Norby, J. Electrochem. Soc. 151 (2004) B669–B678.
[39] S.P. Jiang, S. Zhang, Y.D. Zhen, J. Electrochem. Soc. 153 (2006) A127–A134.
[40] Z. Yang, J.S. Hardy, M.S. Walker, G. Xia, S.P. Simner, J.W. Stevenson, J. Electrochem. Soc. 151 (2004) A1825–A1831.
[41] B. Hua, J. Pu, F. Lu, J. Zhang, B. Chi, L. Jian, J. Power Sources 195 (2010) 2782–2788.
[42] B. Hua, Y. Kong, W. Zhang, J. Pu, B. Chi, L. Jian, J. Power Sources 196 (2011) 7627–7638.
[43] R. Neagu, D. Perednis, A. Princivalle, E. Djurado, Solid State Ionics 177 (2006) 1981–1984.
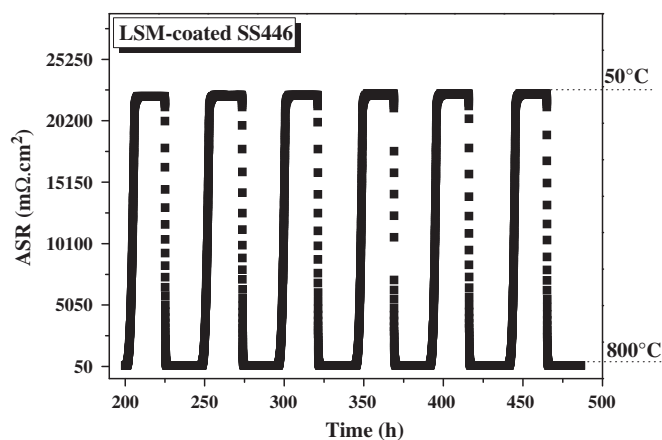
Fig. 10. ASR testing of LSM-coated SS446 alloy during successive thermal cycles (LSM thickness = 300 nm).

[44] R. Neagu, D. Perednis, A. Princivalle, E. Djurado, Solid State Ionics 200 (2006) 6815–6820.
[45] X. Chen, P. Hou, C. Jacobson, S. Visco, L. Dejonghe, Solid State Ionics 176 (2005) 425–433.
[46] E. Konysheva, J. Laatsch, E. Wessel, F. Tietz, N. Christiansen, L. Singheiser, K. Hilpert, Solid State Ionics 177 (2006) 923–930.
[47] N. Orlovskaya, A. Coratolo, C. Johnson, R. Gemmen, J. Am. Ceram. Soc. 87 (2005) 1981–1987.
[48] K.O. Hoyt, P.E. Gannon, P. White, R. Tortop, B.J. Ellingwood, H. Khoshuei, Int. J. Hydrog. Energy 37 (2012) 518–529.
[49] M. Palcut, L. Mikkelsen, K. Neufeld, M. Chen, R. Knibbe, P.V. Hendriksen, J. Hydrog. Energy 37 (2012) 8087–8094.
[50] M. Palcut, L. Mikkelsen, K. Neufeld, M. Chen, R. Knibbe, P.V. Hendriksen, Int. J. Hydrog. Energy 37 (2012) 14501–14510.
[51] P. Piccardo, S. Chevalier, R. Molins, M. Viviani, A. Barbucci, G. Caboche, R. Amendola, S. Fontana, Surf. Coat. Technol. 201 (2006) 4471–4475.
[52] B.C. Church, T.H. Sanders, R.F. Speyer, J.K. Cochran, Mater. Sci. Eng. A 452–453 (2007) 334–340.
[53] Å.H. Persson, L. Mikkelsen, P.V. Hendriksen, M.A.J. Somers, J. Alloys Compd. 521 (2012) 16–29.
[54] K. Huang, P.Y. Hou, J.B. Goodenough, Mater. Res. Bull. 36 (2001) 81–95.
[55] S. Fontana, R. Amendola, S. Chevalier, P. Piccardo, G. Caboche, M. Viviani, R. Molins, M. Sennour, J. Power Sources 171 (2007) 652–662.
[56] N.V. Gavrilov, V.V. Ivanov, A.S. Kamenetskikh, A.V. Nikonov, Surf. Coat. Technol. 206 (2011) 1252–1258.
[57] H.S. Seo, D.W. Yun, K.Y. Kim, Int. J. Hydrog. Energy 38 (2013) 2432–2442.
[58] L. Da Conceição, L. Dessemond, E. Djurado, M.M.V.M. Souza, Int. J. Hydrog. Energy 38 (2013) 15335–15347.
[59] H.S. Seo, D.W. Yun, K.Y. Kim, Int. J. Hydrog. Energy 37 (2012) 16151–16160.
[60] T. Horita, H. Kishimoto, K. Yamaji, Y. Xiong, M.E. Brito, H. Yokokawa, Y. Baba, K. Ogasawara, H. Kameda, Y. Matsuzaki, S. Yamashita, N. Yasuda, T. Uehara, Solid State Ionics 179 (2008) 2216–2221.
[61] T.C. Tsai, A.M. Huntz, C. Dolin, Mater. Sci. Eng. A 212 (1996) 6–13.
[62] Q. Fu, F. Tietz, D. Sebold, E. Wessel, H.-P. Buchkremer, Corros. Sci. 54 (2012) 68–76.
[63] S.W. Sofie, P. Gannon, V. Gorokhovsky, J. Power Sources 191 (2009) 465–472.
[64] X. Xin, S. Wang, J. Qian, C. Lin, Z. Zhan, T. Wen, Int. J. Hydrog. Energy 37 (2012) 471–476.
[65] Y. Xu, Z. Wen, S. Wang, T. Wen, Solid State Ionics 192 (2011) 561–564.
[66] Z.H. Bi, J.H. Zhu, S.W. Du, Y.T. Li, Surf. Coat. Technol. 228 (2013) 124–131.
[67] Z. Yang, G.-G. Xia, X.-H. Li, J.W. Stevenson, Int. J. Hydrog. Energy 32 (2007) 3648–3654.
[68] X. Montero, F. Tietz, D. Sebold, H.P. Buchkremer, A. Ringuedé, M. Cassir, A. Laresgoiti, I. Villareal, J. Power Sources 181 (2008) 172–179.
[69] Z. Yang, G.-G. Xia, G.D. Maupin, J.W. Stevenson, Surf. Coat. Technol. 201 (2006) 4476–4483.
[70] H. Ebrahimifar, M. Zandrazhimi, Solid State Ionics 183 (2011) 171–179.